Available online at www.sciencedirect.com
SCIENCE DIRECT®
International Journal of Heat and Fluid Flow 24 (2003) 399–411
International Journal of HEAT AND FLUID FLOW
www.elsevier.com/locate/ijhff

# Direct numerical simulation of turbulent concentric annular pipe flow Part 2: Heat transfer

Seo Yoon Chung, Hyung Jin Sung *

*Department of Mechanical Engineering, Korea Advanced Institute of Science and Technology, 373-1, Kusong-dong, Yusong-ku, Taejon 305-701, South Korea*

Received 16 April 2002; accepted 17 January 2003

**Abstract**

A direct numerical simulation is performed for turbulent heat transfer in a concentric annulus at $Re_{D_h} = 8900$ and $Pr = 0.71$ for two radius ratios ($R_1/R_2 = 0.1$ and 0.5) and wall heat flux ratio $q^* = 1.0$. Main emphasis is placed on the transverse curvature effect on near-wall turbulent thermal structures. Near-wall turbulent thermal structures close to the inner and outer walls are scrutinized by computing the lower-order statistics. The fluctuating temperature variance and turbulent heat flux budgets are illustrated to confirm the results of the lower-order statistics. Probability density functions of the splat/anti-splat process are investigated to analyze the transverse curvature effect on the strong relationship between sweep and splat events. The present numerical results show that the turbulent thermal structures near the outer wall are more activated than those near the inner wall, which may be attributed to the different vortex regeneration processes between the inner and outer walls.


*Keywords:* Direct numerical simulation; Concentric annular pipe; Turbulent heat transfer; Transverse curvature

## 1. Introduction

Concentric annular pipe is often encountered in engineering applications such as heat exchangers, gas-cooled nuclear reactors and gas turbines. Moreover, study on turbulent heat transfer provides insight into the distinctive feature of the thermal field such as the radial asymmetry of the temperature field. In the preceding paper (Chung et al., 2002), the transverse curvature effect on near-wall turbulent flow structure in a concentric annulus was reported. They showed that overall turbulent statistics near the outer wall were larger than those near the inner wall. The quadrant analysis of the Reynolds shear stress and p.d.f. of the inclination angles of the projected vorticity vectors provided a comprehensive data pertaining to the transverse curvature effect on the turbulence production (consumption). In addition to the study on flow structure, a study on turbulent heat transfer in a concentric annulus is also important from both scientific and engineering viewpoints. In this study, a DNS is performed to elucidate the transverse curvature effect on near-wall turbulent thermal structure in a concentric annulus.

A literature survey reveals that there have been many experimental and numerical studies on turbulent heat transfer in concentric annuli. Heikal et al. (1976) measured wall heat transfer rate in air flow. Kuzay and Scott (1977) measured the wall heat transfer rate and mean temperature in air flow, and they focused on the effect of inner wall rotation. Hasan et al. (1992), Velidandla et al. (1996) and Kang et al. (2001) investigated the buoyancy effect on the velocity and temperature field in a vertical annulus whose inner wall only was heated. They reported that the buoyancy effects were found on the mean and turbulence fields, even at very low values of Richardson number ($Ri = Gr/Re^2$). Numerical simulations of the thermal fields in turbulent flow through concentric annuli with their inner walls heated were performed by many researchers (Wilson and Medwell, 1968; Malik and Pletcher, 1981; Kawamura et al., 1994; Zarate et al., 2001). Wilson and Medwell (1968) used the van Driest model of turbulent viscosity. A constant turbulent Prandtl number $Pr_t = 1$ was used for $Pr > 0.1$, and an

* Corresponding author. Tel.: +82-42-869-3027; fax: +82-42-869-5027.
*E-mail address:* hjsung@mail.kaist.ac.kr (H.J. Sung).

0142-727X/03/$ - see front matter © 2003 Elsevier Science Inc. All rights reserved.
doi:10.1016/S0142-727X(03)00017-1

**Nomenclature**

$a_i$, $b_i$, $c_i$, $d_i$, $e_i$, $f_i$, $g_i$ coefficients of Taylor series ($i = 0, 1, \ldots$)
$C_f$ skin friction coefficient $= \tau_w/(1/2)\rho U_m^2$
$c_p$ specific heat at constant pressure
$D_h$ hydraulic diameter $= 4\delta$
$Gr$ Grashof number
$h$ heat transfer coefficient
$K$ thermal activity ratio $= (\rho_f c_{p_f} \lambda_f/\rho_w c_{p_w} \lambda_w)^{0.5}$
$L_z$ computational length in the $z$ direction
$L_\theta$ computational length in the $\theta$ direction
$Nu_{D_h}$ Nusselt number $= hD_h/\lambda$
$N_r$, $N_\theta$, $N_z$ grid points in the $r$, $\theta$, $z$ directions, respectively
$p$ pressure
$Pr$ Prandtl number $= \nu/\alpha$
$Pr_t$ turbulent Prandtl number $= \nu_t/\alpha_t$
$q''$ wall heat flux
$q^*$ wall heat flux ratio $= q''_o/q''_i$
$q_r$, $q_\theta$, $q_z$ $q_r = r \cdot v_r$, $q_\theta = v_\theta$, $q_z = v_z$
$r$, $\theta$, $z$ spatial coordinates in the $r$, $\theta$, $z$ directions, respectively
$R^*$ radius ratio $= R_1/R_2$
$R_1$, $R_2$ radius of inner and outer cylinder, respectively
$Re$ Reynolds number based on characteristic velocity and length scales
$Re_\delta$ Reynolds number $= U_c\delta/\nu$
$Re_\tau$ Reynolds number $= u_\tau\delta/\nu$
$Re_{\Delta_2}$ Reynolds number $= U_\infty \Delta_2/\nu$
$Re_{D_h}$ Reynolds number $= U_m D_h/\nu$
$Ri$ Richardson number $= Gr/Re^2$
$R_{v'_z v'_z}$ two-point correlations of fluctuating streamwise velocities
$R_{\Theta'\Theta'}$ two-point correlations of fluctuating temperatures
$T$ temperature
$T_m$ bulk mean temperature
$T_r$ dimensionless temperature $= q''/\rho c_p U_m$
$T_\tau$ friction temperature $= q''/\rho c_p u_\tau$
$t$ time
$u_\tau$ friction velocity $= (\tau_w/\rho)^{1/2}$
$U_c$, $U_m$, $U_\infty$ laminar maximum velocity, bulk mean velocity and free stream velocity, respectively
$v_r$, $v_\theta$, $v_z$ velocity components in the $r$, $\theta$, $z$ directions, respectively
$V_r$, $V_\theta$, $V_z$ mean velocity components in the $r$, $\theta$, $z$ directions, respectively
$y$ distance from the inner or outer wall

*Greeks*
$\alpha$ thermal diffusivity $= \lambda/\rho c_p$
$\alpha_t$ eddy diffusivity $= -\overline{v'_r \Theta'}/(\partial\overline{\Theta}/\partial y)$
$\delta$ half-width between inner wall and outer wall
$\Delta_2$ enthalpy thickness
$\Delta r_i$, $\Delta r_o$ minimum grid spacing from the inner and outer wall, respectively
$\Delta r_{max}$ maximum grid spacing in the radial direction
$\Delta\theta$, $\Delta z$ grid spacing in the azimuthal and axial directions, respectively
$\lambda$ thermal conductivity
$\nu$ kinematic viscosity
$\nu_t$ eddy viscosity $= -\overline{v'_r v'_z}/(\partial V_z/\partial y)$
$\rho$ density of fluid
$\tau_w$ statistically averaged wall shear stress at the inner or outer wall
$\Theta$ dimensionless temperature $= (\langle T_w \rangle - T)/T_r$

*Abbreviations*
DNS direct numerical simulation
DS dissipation
LES large eddy simulation
MD molecular diffusion
PD pressure diffusion
p.d.f.s probability density functions
PR production
PS pressure strain
Q1, Q2, Q3, Q4 first, second, third and fourth quadrant, respectively
r.m.s. root mean square
SP splatting parameter $= (1/r)(\partial v'_\theta/\partial\theta) + \partial v'_z/\partial z$
TD turbulent diffusion
TPG temperature–pressure gradient

*Superscripts and subscripts*
$(\ )'$ fluctuating component
$(\ )^+$ normalized by $u_\tau$, $\nu$ or $T_\tau$
$\overline{(\ )}$ statistically averaged in time and space
$(\ )_f$, $(\ )_w$ values of fluid and walls, respectively
$(\ )_i$, $(\ )_o$ values of inner and outer walls, respectively
$(\ )_{rms}$ root mean square value
$\langle\ \rangle$ temporally and spatially averaged in the $\theta$ direction

empirical relation was adopted for $Pr < 0.1$. Malik and Pletcher (1981) evaluated three different turbulence models, and they used a constant turbulent Prandtl number of 0.9. Kawamura et al. (1994) made a LES study with two radius ratios ($R^* = R_1/R_2$). They showed that the Nusselt numbers were in good agreement with the existing correlation of Dalle Donne and Meerwald (1973). They also found the striking similarity between

the velocity and temperature fields. Zarate et al. (2001) compared their numerical results with the experimental data of Kang et al. (2001). They used explicit algebraic heat flux model of So and Sommer (1996) to capture the anisotropy of the turbulent heat flux components.

A perusal of the relevant literature indicates that the information on turbulent heat transfer in concentric annuli with transverse curvature is almost limited. Furthermore, most numerical studies use turbulence models which provide rather limited information. DNS is essential to clarify the transverse curvature effects on turbulent heat transfer considered in this study. With the advent of large scale computers, DNS becomes an important research tool of the turbulent heat transfer. Kim and Moin (1989), Lyons et al. (1991) and Kasagi et al. (1992) performed the DNS studies at moderate Reynolds numbers and Prandtl numbers of about one or less. Later, Kawamura et al. (1998) and Na and Hanratty (2000) studied the effect of Prandtl number on turbulent heat transfer increasing Prandtl number up to 10. All the DNSs mentioned above used isothermal wall boundary conditions for the dimensionless temperature. This leads to the assumption of zero wall temperature fluctuations. However, there exist wall temperature fluctuations on the heated solid wall in real turbulent flow. Study on wall temperature fluctuations can be helpful to understand turbulent heat transport between a flow and a solid wall. For instance, this study can be applied to predict and avoid thermal fatigue failure of solid structures (Kasagi et al., 1989). Lu and Hetsroni (1995) performed DNS of turbulent heat transfer in a open channel flow using ideal isoflux condition. They evaluated many turbulent thermal statistics such as mean temperature, r.m.s. temperature fluctuations and turbulent heat fluxes. They also revealed that the influence of temperature fluctuations at the wall is confined in the very near-wall region. Kong et al. (2000) performed DNS of the developing turbulent thermal boundary layer with two boundary conditions (isothermal and ideal isoflux boundary conditions). Tiselj et al. (2001b) performed DNS of the turbulent flume flow with isothermal and ideal isoflux conditions and analyzed the differences between both types of boundary condition at $Pr = 1$ and 5.4. Tiselj et al. (2001a) studied a conjugate heat transfer problem in turbulent channel flow considering the unsteady conduction in the heated wall. They investigated the change of wall temperature fluctuations varying wall thickness and thermal activity ratio $K = (\rho_f c_{p_f} \lambda_f / \rho_w c_{p_w} \lambda_w)^{0.5}$.

In the present study, which is a sequel to Chung et al. (2002), the transverse curvature effect on turbulent heat transfer in concentric annuli is investigated via DNS. A schematic diagram of the flow and thermal configuration is shown in Fig. 1. Two radius ratios ($R^* = 0.1$ and 0.5) are chosen and the heat flux ratio $q^*$ ($= q_o''/q_i''$) is unity for both radius ratios. The flow conditions are the same as those of Chung et al. (2002). Many turbulent thermal statistics with ideal isoflux boundary conditions are obtained to analyze the near-wall thermal structures close to the inner and outer walls, which are compared with the previous DNS data of turbulent heat transfer. The budgets of temperature variance and turbulent heat fluxes are computed to explain the different turbulent statistics between near inner and outer walls. Finally, p.d.f.s of splat/anti-splat process are performed to shed further light on the transverse curvature effects on the flow and thermal fields in concentric annuli.

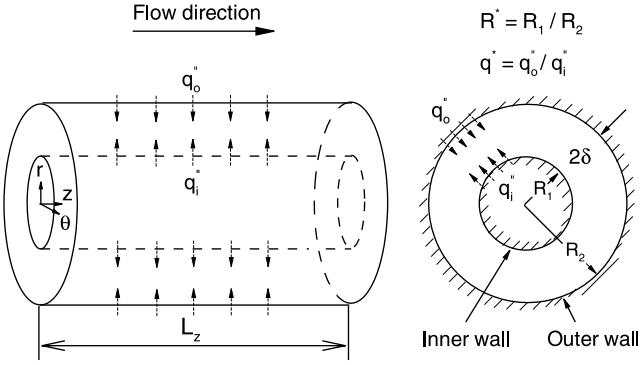


Fig. 1. Schematic diagram and coordinate system.

## 2. Numerical procedure

The computational domain is shown in Fig. 1. The transverse curvature effect on near-wall turbulent thermal structure is analyzed for two radius ratios ($R^* = 0.1$ and 0.5) and the heat flux ratio $q^*$ of 1.0 for both radius ratios. The Reynolds number based on the bulk velocity $U_m$ and the hydraulic diameter $D_h$ is $Re_{D_h} = 8900$ and the Prandtl number is $Pr = 0.71$. The computational length in the axial direction is $L_z = 25\delta$ and $30\delta$ for $R^* = 0.1$ and 0.5, respectively. Any buoyancy effect is neglected, and hence temperature is considered as a passive scalar. Periodic boundary conditions for velocity and temperature components are applied in the streamwise and circumferential directions. Heating conditions at both walls are the same as those of Kasagi et al. (1992). Due to the heating conditions, the temperature ensemble-averaged over the $\theta$ direction and time $\langle T \rangle$ should increase linearly in the streamwise direction, i.e.,

$$\frac{\partial \langle T \rangle}{\partial z} = \frac{\partial \langle T_m \rangle}{\partial z} = \frac{\partial \langle T_w \rangle}{\partial z} = \text{const.} \tag{1}$$

The dimensionless temperature $\Theta_i$ or $\Theta_o$ is defined to use periodic conditions for in the $\theta$ and $z$ directions. $\Theta_i$ and $\Theta_o$ are expressed as follows:

$$\begin{aligned} \Theta_i &= (\langle T_{w_i} \rangle - T)/T_{r_i}, \\ \Theta_o &= (\langle T_{w_o} \rangle - T)/T_{r_o}, \end{aligned} \tag{2}$$

where $T_m$ and $T_w$ denote mean temperature of fluid and wall temperature, respectively. Here, $T_{r_i}$ and $T_{r_o}$ are defined as $T_{r_i} = q''_i/\rho c_p U_m$ and $T_{r_o} = q''_o/\rho c_p U_m$, respectively. A no-slip boundary condition is imposed at the wall for the velocity components and an ideal isoflux condition is used for the temperature component.

The continuity and Navier–Stokes equations in cylindrical coordinates are the same as Chung et al. (2002). When the variables $q_r = r \cdot v_r$, $q_\theta = v_\theta$ and $q_z = v_z$ are introduced, the energy equations regarding $\Theta_i$ can be written as:

$$\frac{\partial \Theta_i}{\partial t} + \frac{1}{r}\frac{\partial q_r \Theta_i}{\partial r} + \frac{1}{r}\frac{\partial q_\theta \Theta_i}{\partial \theta} + \frac{\partial q_z \Theta_i}{\partial z} - \frac{1}{T_{r_i}}\frac{\partial \langle T_{w_i}\rangle}{\partial z} q_z = \frac{1}{RePr}\left[\frac{1}{r}\frac{\partial}{\partial r}\left(r\frac{\partial \Theta_i}{\partial r}\right) + \frac{1}{r^2}\frac{\partial^2 \Theta_i}{\partial \theta^2} + \frac{\partial^2 \Theta_i}{\partial z^2}\right] \quad (3)$$

with

$$\frac{1}{T_{r_i}}\frac{\partial \langle T_{w_i}\rangle}{\partial z} = \frac{2(q^* + R^*)}{R_2/\delta(1 - R^{*2})}. \quad (4)$$

Here, $v_r$, $v_\theta$, $v_z$ denote the radial, azimuthal and axial velocity components, respectively. All the variables are non-dimensionalized by a characteristic length $\delta$, velocity scale $U_c$, and temperature scale. Here, $U_c$ is the laminar maximum velocity. For the flow field, the numerical method of Kim et al. (2002) is adopted and the second-order Crank–Nicolson method in time is applied for all the terms of the energy equation. All the terms of the governing equations are resolved with a second-order central difference scheme in space with a staggered mesh.

Figs. 2 and 3 exhibit the two-point correlations of the fluctuating streamwise velocities and temperatures in the

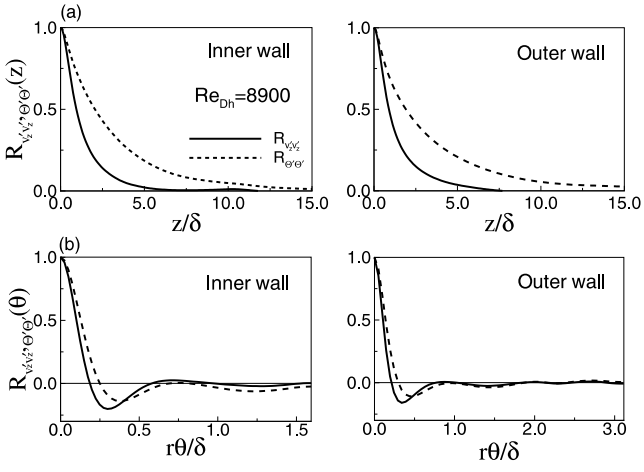


Fig. 2. Two-point correlation coefficients of streamwise velocity fluctuations and temperature fluctuations for $R^* = 0.5$: (a) streamwise separations, (b) azimuthal separations.

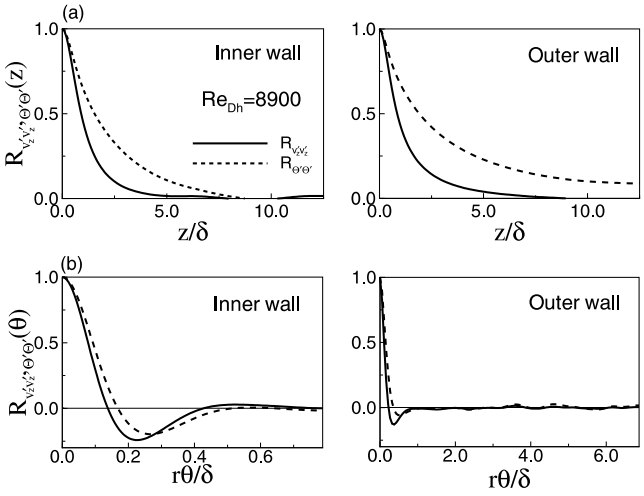


Fig. 3. Two-point correlation coefficients of streamwise velocity fluctuations and temperature fluctuations for $R^* = 0.1$: (a) streamwise separations, (b) azimuthal separations.

$z$ and $\theta$ directions. Here, the two-point correlations are calculated at $y^+ \approx 5$. For the axial velocities, the auto-correlations in Figs. 2 and 3 show that they fall off to zero values for separations. This suggests that the computational domains are sufficiently large to simulate the largest eddies in the flow. For the temperature fluctuations, the streamwise two-point correlations in Figs. 2(a) and 3(a) do not decay to zero in the computational domain (0.09 and 0.03 for $R^* = 0.1$ and 0.5, respectively). The previous DNS study of Tiselj et al. (2001a) with the same thermal boundary condition of the present one indicates that the periodicity length, which is long enough for the velocity field, is long enough also for the passive scalar fields. This guarantees that the computational domain used in the present work is adequate to capture the largest thermal structures. The computation is conducted in only one-quarter of the full cross-section in the azimuthal direction for $R^* = 0.5$ as in the simulation of Chung et al. (2002). The use of periodic thermal boundary conditions in the $\theta$ directions is justified by examining the two-point correlations as shown in Figs. 2(b) and 3(b). In Figs. 2(b) and 3(b), the negative peaks of the auto-correlation functions for temperature shift to smaller values of $\theta$ than those for axial velocities because of the isoflux boundary conditions. This tendency exemplified larger thermal streaky structures as pointed out in the previous studies (Tiselj et al., 2001b). The detailed grid resolutions for two radius ratios are summarized in Table 1. A hyperbolic tangent function is used for a clustering of grid points in the wall-normal direction. The computational time step is $0.035\delta/U_c$ and $0.04\delta/U_c$ for $R^* = 0.1$ and 0.5, respectively, and the total averaging time to obtain the statistics is $700\delta/U_c$ and $800\delta/U_c$ for $R^* = 0.1$ and 0.5, respectively.

Table 1
Grid resolutions

| | | |
|---|---|---|
| $R^*$ | 0.5 | 0.1 |
| $q^*$ | 1.0 | 1.0 |
| $L_z^+$ | 4553.71 | 4485.75 |
| $L_{\theta_i}^+$ | 476.86 | 250.53 |
| $L_{\theta_o}^+$ | 908.85 | 1995.54 |
| $\Delta z^+$ | 14.23 | 17.52 |
| $(R_1\,\Delta\theta)^+$ | 3.73 | 0.98 |
| $(R_2\,\Delta\theta)^+$ | 7.10 | 7.80 |
| $\Delta r_i^+$ | 0.13 | 0.15 |
| $\Delta r_o^+$ | 0.12 | 0.12 |
| $\Delta r_{max}^+$ | 12.89 | 15.23 |
| $(N_r, N_\theta, N_z)$ | (65, 128, 320) | (65, 256, 256) |

## 3. Results and discussion

### 3.1. Mean flow and thermal properties

Before proceeding further, it would be advantageous to look into the characteristics of mean thermal properties. Mean flow and thermal parameters are listed in Table 2. Here, $Re_\delta$ is based on the laminar maximum velocity $U_c$ and the half-width $\delta$ between the inner and outer walls. In Table 2, the skin friction coefficient ($C_f = \tau_w/(1/2)\rho U_m^2$) of the inner wall is larger than that of the outer wall as in the case of Chung et al. (2002). Moreover, this tendency becomes more clear as $R^*$ decreases. Note that the Nusselt number based on the hydraulic diameter $Nu_{D_h}$ of the inner wall is also larger than that of the outer wall. Difference in the value of the Nusselt number between the inner and outer walls becomes more clear due to the heat flux ratio. A comparison is made of the mean temperature distributions normalized by the friction temperature ($T_\tau = q''/\rho c_p u_\tau$) with the DNS data of Kasagi et al. (1992) as shown in Fig. 4. A best-fit of the thermal law of the wall in the logarithmic region is estimated from the dimensionless temperature gradient. In the case of the outer profiles, agreement with the previous DNS data of Kasagi et al. (1992) is satisfactory in spite of the different thermal boundary conditions. This verifies that the boundary condition for temperature does not affect the mean temperature field (Tiselj et al., 2001b). It is interesting to note that there is a slight discrepancy between the profiles of the inner and outer walls near $y^+ > 70$ in Fig. 4(a). The deviations are significant in Fig. 4(b). This may be attributed to the curvature effect, which is caused by the decrease of the radius of the inner cylinder (Chung et al., 2002).

Table 2
Mean parameters

| | | |
|---|---|---|
| $R^*$ | 0.5 | 0.1 |
| $q^*$ | 1.0 | 1.0 |
| $Re_{D_h}$ | 8900 | 8900 |
| $Re_\delta$ | 3355 | 3487 |
| $Re_\tau$ (inner) | 152 | 179 |
| $Re_\tau$ (outer) | 144 | 143 |
| $C_f$ (inner) | 0.01006 | 0.01300 |
| $C_f$ (outer) | 0.00913 | 0.00825 |
| $Nu_{D_h}$ (inner) | 35.03 | 62.55 |
| $Nu_{D_h}$ (outer) | 28.51 | 27.63 |

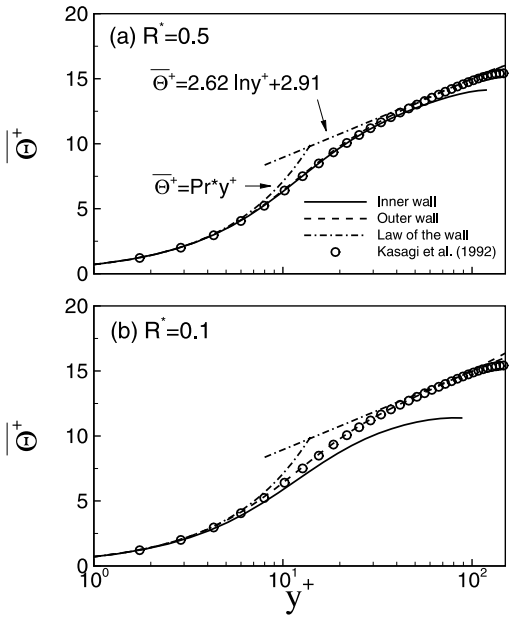


Fig. 4. Mean temperature distributions.

### 3.2. Root-mean-square temperature fluctuations and turbulent heat flux

The r.m.s. temperature fluctuations normalized by the friction temperature of each wall are compared with the previous results in Fig. 5. Here, the data obtained by Kong et al. (2000) is the result for $Re_{\Delta_2} = 361$. Note that the r.m.s. temperature fluctuations at the walls yield non-zero values due to the isoflux boundary conditions. The wall temperature fluctuations of Kasagi et al. (1992) which used the isothermal condition are zero. On the other hand, the wall temperature fluctuations have a constant value (≈2.0–2.2), independent of the Reynolds number range of the studies which employed the isoflux conditions. In the outer region, the profiles of the r.m.s. temperature fluctuations are different from each other owing to the Reynolds number effect. A comparison between the inner and outer walls indicates that the values of the outer walls are larger than those of the inner walls. As mentioned in the study of Chung et al. (2002), the outer wall supplies relatively more turbulent kinetic energy than the inner wall to the same volume due to the transverse curvature effect.

The axial and wall-normal turbulent heat fluxes are exhibited in Figs. 6 and 7, respectively. In Fig. 7, $v_r$

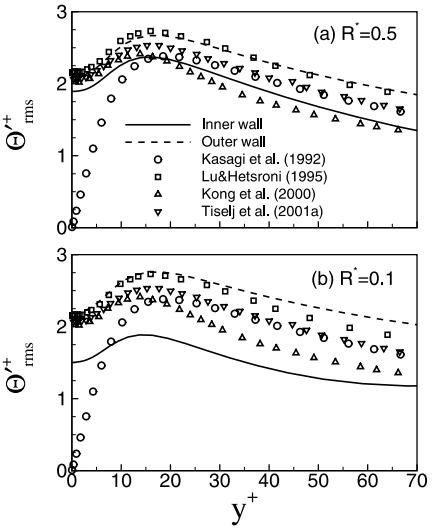


Fig. 5. Root-mean-square temperature fluctuations.

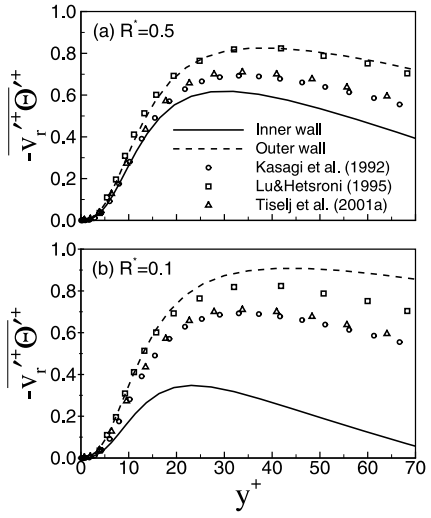


Fig. 7. Distributions of turbulent wall-normal heat flux.

denotes a velocity component normal to the each wall. It is seen that the values of axial turbulent heat fluxes near the outer walls are in general agreement with the previous results (Kasagi et al., 1992; Lu and Hetsroni, 1995; Tiselj et al., 2001a) in Fig. 6. On the other hand, some discrepancy among the results appears in the case of wall-normal turbulent heat fluxes and there is a tendency to get higher value with increasing Reynolds number. It should be noted that the results near the inner walls are smaller than those near the outer walls like the r.m.s. distributions of fluctuating temperature in Figs. 6 and 7.

The wall-normal heat flux ($-\overline{v_r'^+\Theta'^+}$) and total heat flux ($((1/Pr)(\mathrm{d}\overline{\Theta}^+/\mathrm{d}y^+) - \overline{v_r'^+\Theta'^+}$) in the global coordinate are displayed in Fig. 8. Here, $y$ and $v_r$ denote a distance from the inner wall and a velocity component normal to the inner wall, respectively. It is interesting to note that the distributions of wall-normal heat flux and total heat flux are asymmetric and curvilinear as in the case of total shear stress in Chung et al. (2002). Furthermore, the positions of zero total heat flux are closer to the inner walls than those of the total shear stress (0.61 and 0.88 for $R^* = 0.1$ and 0.5, respectively) in the previous study of Chung et al. (2002). This phenomenon is attributed to the heat flux ratio ($q^* = q_o''/q_i''$) of 1 prescribed in this study.

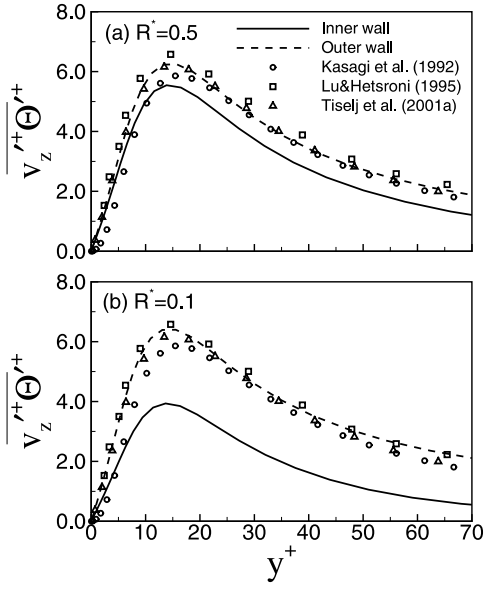


Fig. 6. Distributions of turbulent axial heat flux.

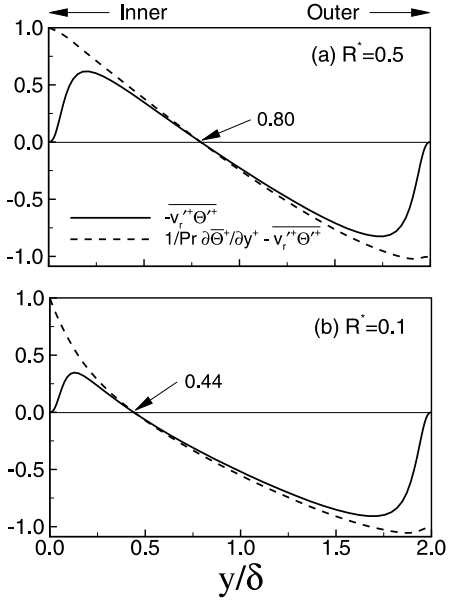


Fig. 8. Distributions of turbulent wall-normal heat flux and total heat flux.

### 3.3. Limiting behaviors of turbulent statistics

To analyze the near-wall asymptotic behavior of the turbulent thermal statistics, we expand the velocity and temperature in Taylor series. Considering the continuity and dynamic equations under the no-slip and isothermal boundary conditions, $V_z$, $v_r'$, $v_z'$, $\overline{\Theta}$ and $\Theta'$ are expressed in the following form (Kong et al., 2000):

$$\begin{aligned} V_z &= a_1 y + a_4 y^4 + \cdots, \\ v_z' &= b_1 y + b_2 y^2 + \cdots, \\ v_r' &= c_2 y^2 + c_3 y^3 + \cdots, \\ \overline{\Theta} &= d_0 + d_1 y + d_4 y^4 + \cdots, \\ \Theta' &= e_1 y + e_3 y^3 + \cdots, \end{aligned} \tag{5}$$

where the coefficients $a_i$, $b_i$, $c_i$, $d_i$, $e_i$ $(i = 0, 1, \ldots)$ are functions of $\theta$, $z$ and $t$. Here, $y$ denotes the distance from the each wall. In the case of isoflux wall, the mean and fluctuating dimensionless temperatures are written as follows:

$$\begin{aligned} \overline{\Theta} &= f_0 + f_1 y + f_3 y^3 + \cdots, \\ \Theta' &= g_0 + g_1 y + g_3 y^3 + \cdots \end{aligned} \tag{6}$$

Near-wall behaviors of the turbulent eddy viscosity ($\nu_t = -\overline{v_r' v_z'}/(\partial V_z/\partial y)$) and eddy diffusivity ($\alpha_t = -\overline{v_r' \Theta'}/(\partial\overline{\Theta}/\partial y)$) are shown in Figs. 9 and 10, respectively. The turbulent eddy viscosity and eddy diffusivity can be expressed in the following forms, considering isothermal boundary condition in Eq. (5):

$$\begin{aligned} \nu_t &= -\frac{\overline{b_1 c_2}}{a_1} y^3 + \cdots, \\ \alpha_t &= -\frac{\overline{c_2 e_1}}{d_1} y^3 + \cdots \end{aligned} \tag{7}$$

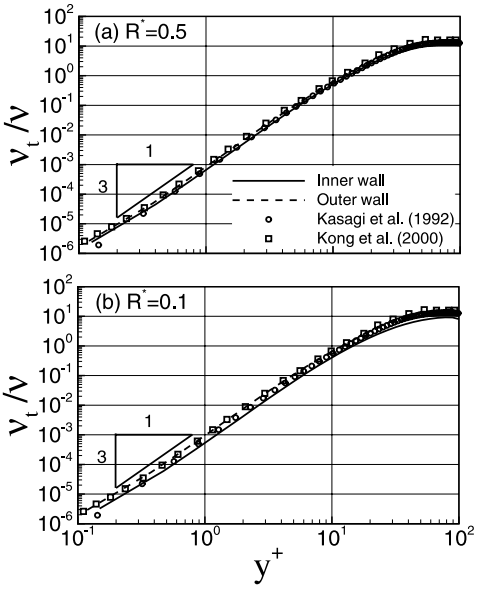


Fig. 9. Near-wall behavior of turbulent eddy viscosity.

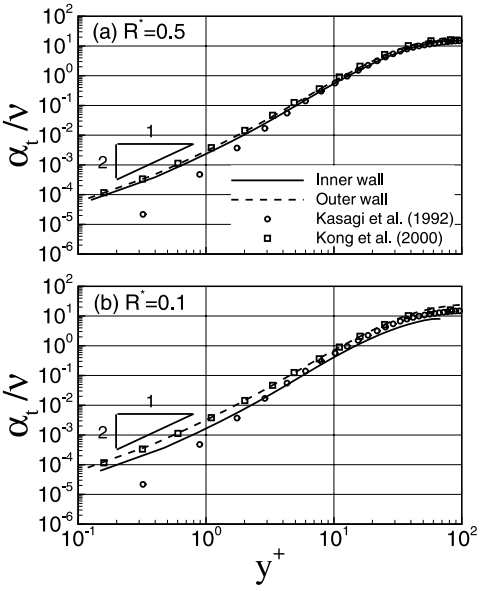


Fig. 10. Near-wall behavior of turbulent eddy diffusivity.

On the other hand, substituting Eq. (6) into the expression of the turbulent eddy diffusivity yields

$$\alpha_t = -\frac{\overline{c_2 g_0}}{f_1} y^2 + \cdots \tag{8}$$

It is indicated that the turbulent eddy viscosity and eddy diffusivity are proportional to $y^3$ and $y^2$ as shown in Figs. 9 and 10, respectively. These are predicted well compared with the result of Kong et al. (2000). In the very close to the wall, the distributions of the turbulent eddy viscosity and eddy diffusivity deviate slightly from $y^3$ and $y^2$, respectively. This is because the wall-normal velocity does not exactly satisfy $\partial v_r'/\partial y = 0$ at the wall in a finite difference method (Kong et al., 2000).

### 3.4. Correlations between velocity and temperature

In this subsection, we consider the cross-correlation coefficients between velocity and temperature to give the quantitative measures for the interconnection between the thermal and kinematic characteristics of the turbulent fluctuations. The correlation coefficients between temperature and axial velocity fluctuations are shown in Fig. 11. The higher value of Kasagi et al. (1992) in the region of $y^+ < 12$ demonstrates that a strong similarity can be seen in the use of the isothermal conditions. Away from the wall ($y^+ > 45$), the inner wall case shows a significant reduction in the correlation coefficient for $R^* = 0.1$. This suggests that the coherent thermal structure near the inner wall is relatively weak due to the transverse curvature effect.

The correlation coefficients between temperature and wall-normal velocity fluctuations are depicted in Fig. 12.

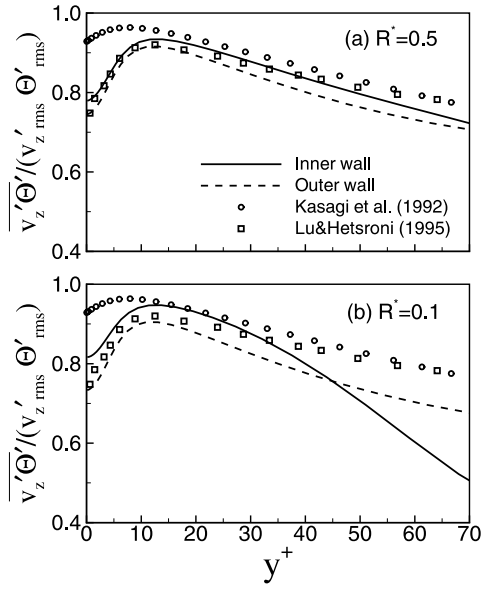


Fig. 11. Profiles of the correlation coefficients between fluctuations of streamwise velocity and temperature.

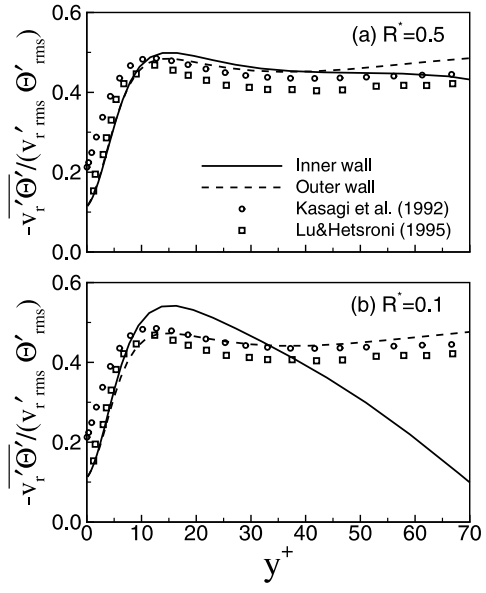


Fig. 12. Profiles of the correlation coefficients between fluctuations of wall-normal velocity and temperature.

As shown in Fig. 11, the wall-normal velocity and temperature fluctuations of Kasagi et al. (1992) are better correlated than those of other studies due to the thermal boundary conditions. Close to the wall ($y^+ <$ 30–40), the profiles of the inner walls are higher than those of the outer walls. Away from the walls, the profiles near the inner walls show less correlations than those near the outer walls. This tendency is more pronounced as $R^*$ decreases, which is also related to the assertion in Fig. 11 as mentioned above.

### 3.5. Budgets of temperature variance and heat fluxes

One main advantage of DNS is to compute the various terms in the budgets of the turbulent transport equations that are difficult to measure. The budget data obtained by DNS give detailed information to evaluate the turbulence models and these are of great help to the new turbulence modeling (Mansour et al., 1988). All derivatives of mean quantities except the axial velocity are zero in the streamwise and azimuthal directions, considering $\partial\langle T\rangle/\partial z = \text{const}$. The remaining terms of the budgets in the fluctuating temperature variance $\overline{\Theta_i'^2}/2$ and turbulent heat fluxes $\overline{v_z'\Theta_i'}/\overline{v_r'\Theta_i'}$ in cylindrical coordinates are as follows:

$\overline{\Theta_i'^2}/2$-budget:

$$0 = \underbrace{-\overline{v_r'\Theta_i'}\frac{\partial\overline{\Theta}_i}{\partial r} + \frac{\overline{v_r'\Theta_i'}}{T_{r_i}}\frac{\partial\langle T_{w_i}\rangle}{\partial z}}_{\text{PR}} \underbrace{-\frac{1}{2r}\frac{\partial}{\partial r}(r\overline{v_r'\Theta_i'^2})}_{\text{TD}} + \underbrace{\frac{1}{2RePr}\frac{1}{r}\frac{\partial}{\partial r}\left(r\frac{\partial\overline{\Theta_i'^2}}{\partial r}\right)}_{\text{MD}} \underbrace{-\frac{1}{RePr}\left[\overline{\left(\frac{\partial\Theta_i'}{\partial r}\right)^2} + \overline{\frac{1}{r^2}\left(\frac{\partial\Theta_i'}{\partial\theta}\right)^2} + \overline{\left(\frac{\partial\Theta_i'}{\partial z}\right)^2}\right]}_{\text{DS}}; \tag{9}$$

$\overline{v_z'\Theta_i'}$-budget:

$$0 = \underbrace{-\overline{v_r'\Theta_i'}\frac{\partial V_z}{\partial r} - \overline{v_r'v_z'}\frac{\partial\overline{\Theta}_i}{\partial r} + \frac{\overline{v_r'^2}}{T_{r_i}}\frac{\partial\langle T_{w_i}\rangle}{\partial z}}_{\text{PR}} \underbrace{-\frac{1}{r}\frac{\partial}{\partial r}(r\overline{v_r'v_z'\Theta_i'})}_{\text{TD}} + \underbrace{\overline{\Theta_i'\frac{\partial p'}{\partial z}}}_{\text{TPG}} + \underbrace{\frac{1}{Re}\frac{1}{r}\frac{\partial}{\partial r}\left(r\overline{\Theta_i'\frac{\partial v_z'}{\partial r}}\right) + \frac{1}{RePr}\frac{1}{r}\frac{\partial}{\partial r}\left(r\overline{v_z'\frac{\partial\Theta_i'}{\partial r}}\right)}_{\text{MD}} \underbrace{-\frac{1}{Re}\left(1+\frac{1}{Pr}\right)\left[\overline{\left(\frac{\partial v_z'}{\partial r}\right)\left(\frac{\partial\Theta_i'}{\partial r}\right)} + \overline{\frac{1}{r^2}\left(\frac{\partial v_z'}{\partial\theta}\right)\left(\frac{\partial\Theta_i'}{\partial\theta}\right)} + \overline{\left(\frac{\partial v_z'}{\partial z}\right)\left(\frac{\partial\Theta_i'}{\partial z}\right)}\right]}_{\text{DS}}; \tag{10}$$

$\overline{v_r'\Theta_i'}$-budget:

$$0 = \underbrace{-\overline{v_r'^2}\frac{\partial\overline{\Theta}_i}{\partial r} + \frac{\overline{v_r'v_z'}}{T_{r_i}}\frac{\partial\langle T_{w_i}\rangle}{\partial z}}_{\text{PR}} \underbrace{-\frac{1}{r}\frac{\partial}{\partial r}(r\overline{v_r'^2\Theta_i'})}_{\text{TD}} + \underbrace{\frac{\overline{v_\theta'^2\Theta_i'}}{r}}_{\text{PD}} \underbrace{-\frac{\partial\overline{p'\Theta_i'}}{\partial r}}_{\text{PD}} + \underbrace{\overline{p'\frac{\partial\Theta_i'}{\partial r}}}_{\text{PS}} + \underbrace{\frac{1}{Re}\left[\frac{1}{r}\frac{\partial}{\partial r}\left(r\overline{\Theta_i'\frac{\partial v_r'}{\partial r}}\right) - \frac{\overline{v_r'\Theta_i'}}{r^2}\right] + \frac{1}{RePr}\frac{1}{r}\frac{\partial}{\partial r}\left(r\overline{v_r'\frac{\partial\Theta_i'}{\partial r}}\right)}_{\text{MD}} \underbrace{-\frac{2}{Re}\frac{1}{r^2}\overline{\Theta_i'\frac{\partial v_\theta'}{\partial\theta}}}_{\text{DS}} \underbrace{-\frac{1}{Re}\left(1+\frac{1}{Pr}\right)\left[\overline{\left(\frac{\partial v_r'}{\partial r}\right)\left(\frac{\partial\Theta_i'}{\partial r}\right)} + \overline{\frac{1}{r^2}\left(\frac{\partial v_r'}{\partial\theta}\right)\left(\frac{\partial\Theta_i'}{\partial\theta}\right)} + \overline{\left(\frac{\partial v_r'}{\partial z}\right)\left(\frac{\partial\Theta_i'}{\partial z}\right)}\right]}_{\text{DS}}. \tag{11}$$

The terms on the right-hand sides of Eqs. (9)–(11) are identified as follows: production PR, turbulent diffusion

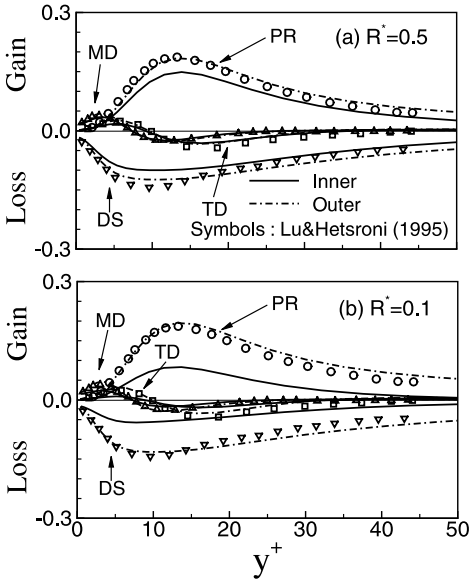


Fig. 13. Budget of fluctuating temperature variance $\overline{\Theta'^2}/2$.

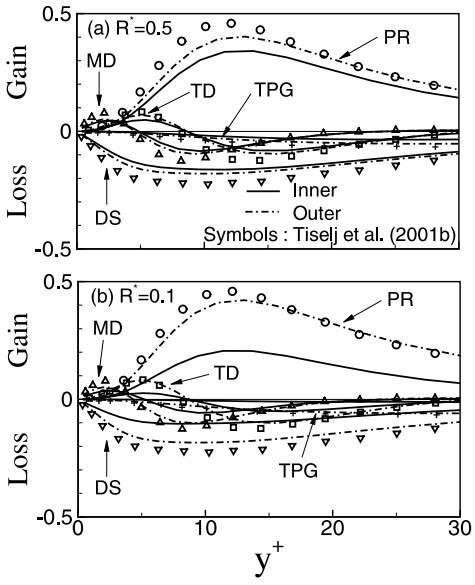


Fig. 14. Budget of turbulent axial heat flux $\overline{v'_z\Theta'}$.

TD, pressure strain PS, pressure diffusion PD, molecular diffusion MD and dissipation DS. The two pressure terms can be combined to the temperature–pressure gradient term TPG.

The budgets for the fluctuating temperature variance ($\overline{\Theta'^2}/2$) are displayed in Fig. 13. A comparison is made of $\overline{\Theta'^2}/2$ with the DNS data of Lu and Hetsroni (1995) which are obtained under the same boundary condition of the present study. The present prediction near the outer wall is in good agreement with the data of Lu and Hetsroni (1995). The MD and DS terms which are relatively smaller than those of Kasagi et al. (1992) [not shown] are important in the vicinity of the walls. It is also demonstrated that the MD and TD terms play important roles at $y^+ < 30$, and the PR and DS terms are in local balance for $y^+ > 30$. Note that the values near the outer walls are larger than those near the inner walls, and this tendency becomes more clear in the PR and DS terms.

Examination of the budgets of the turbulent heat flux indicates the contributions of various processes to the turbulent heat flux. The budgets of the turbulent axial heat flux ($\overline{v'_z\Theta'}$) are exhibited in Fig. 14. Here, symbols are used for the data of Tiselj et al. (2001b) for $Pr = 1.0$ to compare with the present ones. The difference between the profiles of Tiselj et al. (2001b) and the present study can be attributed to the effects of the Reynolds numbers and the Prandtl numbers. At the wall, the MD and DS terms are important, and these are small in comparison with the results of Kasagi et al. (1992) under the isothermal boundary conditions [not shown]. It is seen that the PR and DS terms play major roles throughout the layer, and the TPG terms become large away from the walls.

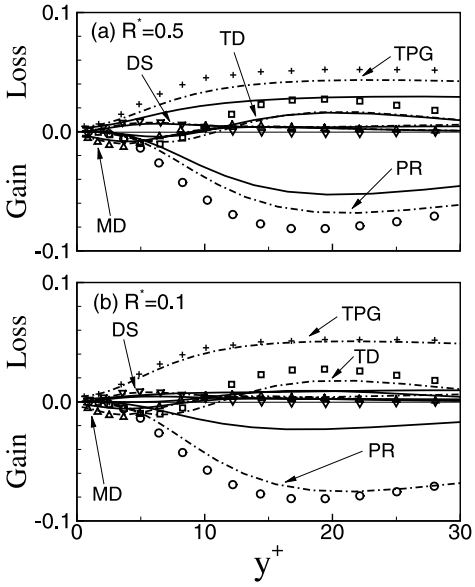


Fig. 15. Budget of turbulent wall-normal heat flux $\overline{v'_r\Theta'}$. See Fig. 14 for legend.

The budgets of the turbulent wall-normal heat flux ($\overline{v'_r\Theta'}$) are shown in Fig. 15. An inconsistency in the TD and PR terms between the data of Tiselj et al. (2001b) and the present study is associated with the different Prandtl numbers as stated in Fig. 14. Unlike the turbulent axial heat flux case, the TPG and PR terms are dominant. An examination of the results in Figs. 14–17 indicates that the values near the outer walls are larger than those near the inner walls. This reconfirms the results of turbulent thermal statistics such as the r.m.s. temperature fluctuations and the turbulent heat flux.

### 3.6. Splat/anti-splat process

The key feature to note in this study is that the turbulent thermal statistics near the outer wall are larger than those near the inner wall as in the simulation of a concentric annular pipe flow by Chung et al. (2002). This suggests a strong similarity between the flow and thermal fields. Chung et al. (2002) did the quadrant analysis of the Reynolds shear stress to elucidate the transverse curvature effects on the flow field in a concentric annulus. In the quadrant analysis of the Reynolds shear stress of Chung et al. (2002), sweep events near the outer walls were more predominant than those near the inner walls. On the other hand, ejections near the inner walls contributed to the Reynolds shear stress more predominantly than those near the outer walls. Splatting mechanism is considered as one of the ingredients which are closely linked to the sweep events near the wall. The splatting is defined as a net energy transfer from the vertical component ($v_r'$) of turbulence intensity to the horizontal ones ($v_\theta'$ and $v_z'$) (Moin and Kim, 1982). The splatting effect, which is correlated with the sweep events and vorticity stretching, produces a flow pattern similar to that of a jet impinging upon a wall. In the present study, we develop a detailed explanation for the altered splatting effect in the flow due to the transverse curvature by a quantitative investigation. To the best of our knowledge, there has been no comparative study on a quantitative approach to the splatting mechanism.

The PS terms in the budget of $\overline{v_r'^2}$ have been exploited to explain the splatting effect in the previous studies (Moin and Kim, 1982; Mansour et al., 1988; Eggels et al., 1994). Fig. 16 shows the PS terms in the budget of $\overline{v_r'^2}$. The reversal of the sign of the PS term near the wall ($y^+ < 12$) indicates the presence of splatting effect clearly. It is interesting to note that the values near the inner walls are smaller than those near the outer walls. This reflects stronger splatting events near the outer walls because of the transverse curvature.

To explain the difference in the strength of splatting events between inner and outer walls clearly, the p.d.f.s of splat/anti-splat process are carried out. The p.d.f. investigation of splat/anti-splat event is performed under the same flow condition (computational domain and grid resolution) presented by Chung et al. (2002). Here, a splat event transfers energy from the normal velocity component to the two tangential velocity ones, and an anti-splat event is a counterpart of a splat one (Perot and Moin, 1995). We follow the approach of Shen et al. (1999) which employ the parameter $((1/r)(\partial v_\theta'/\partial\theta) + \partial v_z'/\partial z$, hereinafter referred to as SP) from the continuity equation. SP denotes a positive value in the case of splat event, on the other hand, it has a negative value in the case of anti-splat event.

The p.d.f.s of the splat/anti-splat process for $R^* = 0.1$, weighted by the absolute value of SP normalized by its r.m.s. value, are shown in Fig. 17. In the horizontal axes of the pictures, the superscript ($^*$) denotes that the quantity is normalized by its r.m.s. value. The weighted p.d.f.s enhance the contributions of the strong splatting

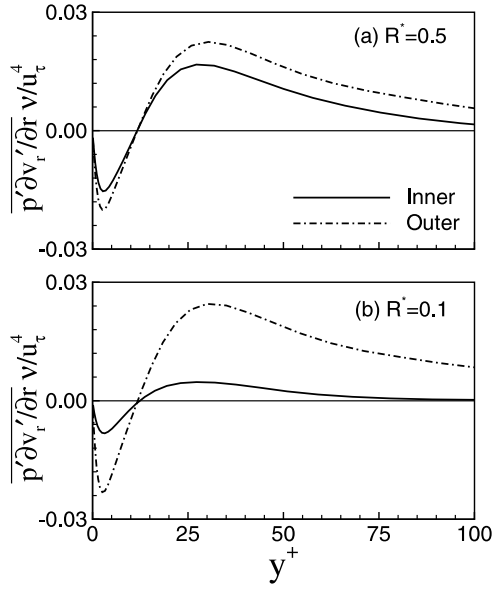


Fig. 16. PS terms in the budget of $\overline{v_r'v_r'}$.

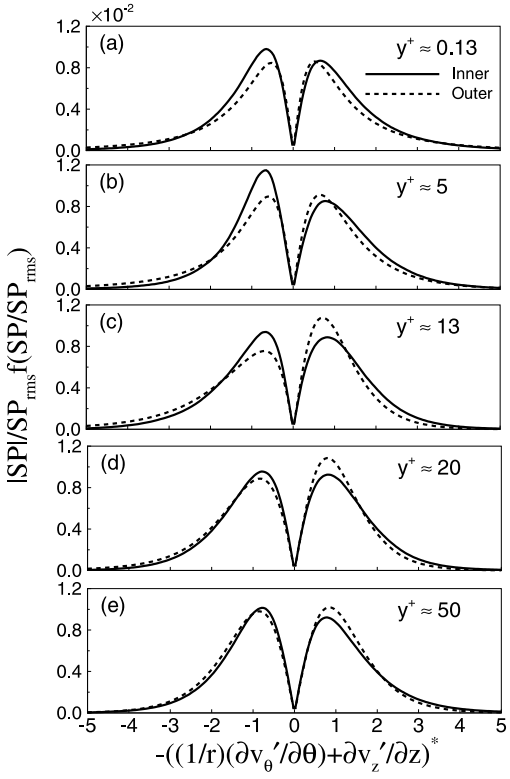


Fig. 17. Weighted p.d.f.s of the splat/anti-splat process for $R^* = 0.1$.

events. The distributions near the inner and outer walls are similar to those near the outer walls for $R^* = 0.5$ [not shown], while the significant discrepancies are found for $R^* = 0.1$. It should be pointed out that the splat events near the outer walls are stronger than those near the inner walls in Fig. 17(a) and (b). This illustrates the point discussed by Chung et al. (2002) that the sweep events near the outer walls are stronger than those near the inner walls. On the contrary, in Fig. 17(c) and (d), the profiles of the inner walls are larger than those of the outer walls in the strong anti-splat region. This leads to stronger ejection events near the inner walls. To attain an in-depth explanation for the close relation between sweep/ejection and splat/anti-splat events, the p.d.f.s of the splat/anti-splat process about each quadrant of the Reynolds shear stress are performed.

The p.d.f.s of the splat/anti-splat process about each quadrant of the Reynolds shear stress are demonstrated in Figs. 18 and 19. Here, $Q_j$ ($j = 1$–$4$) represents each quadrant according to the signs of $v_r'$ and $v_z'$ (Chung et al., 2002). The thin and thick lines denote the profiles of the inner and outer walls, respectively. At the closest point to the wall ($y^+ \approx 0.13$), the distributions of Q3/Q4 and Q1/Q2 are highly concentrated in the strong splat and anti-splat regions, respectively, due to the wall proximity effect. This tendency becomes weak away from the walls. Note that the profiles of Q2 and Q4 are

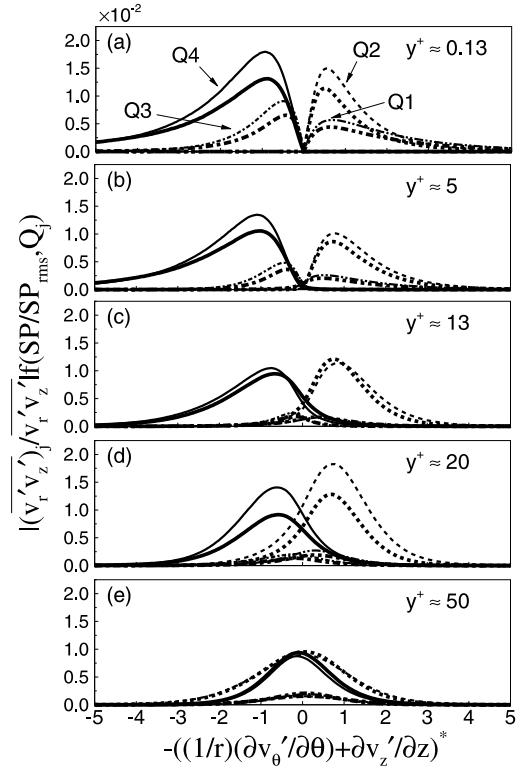


Fig. 18. Weighted p.d.f.s of the splat/anti-splat process regarding each quadrant of Reyonlds shear stress for $R^* = 0.5$.

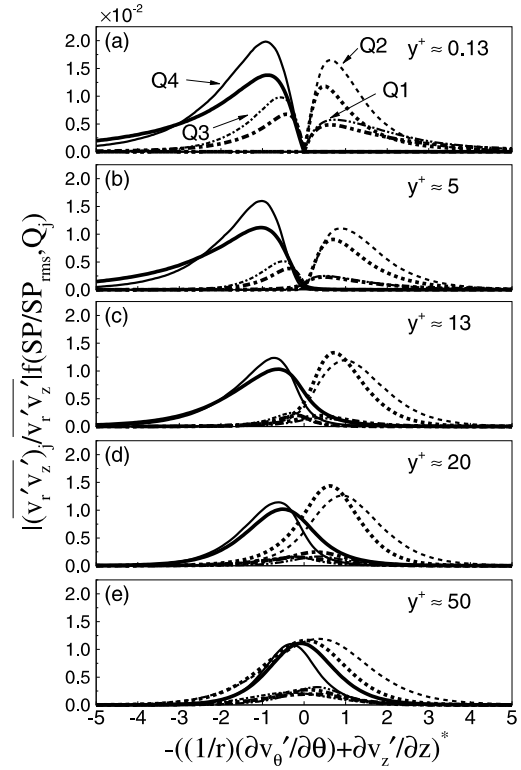


Fig. 19. Weighted p.d.f.s of the splat/anti-splat process regarding each quadrant of Reyonlds shear stress for $R^* = 0.1$.

larger than those of Q1 and Q3. This is consistent with the result of the quadrant analysis for the Reynolds shear stress by Chung et al. (2002). In the distributions of Q4 in Fig. 19(a) and (b), stronger splat events can be seen near the outer walls. On the other hand, the Q2 profiles of inner walls in the strong anti-splat region are larger than those of outer walls in Fig. 19(c) and (d). This is not pronounced in the case of $R^* = 0.5$. Figs. 18 and 19 give a sufficiently complete picture of the strong connection between sweep and splat events, or between ejection and anti-splat events.

As discussed above, it is clearly seen that strong splat events, which are closely linked to the strong sweep ones, can be observed near the outer walls more frequently. This allows easier comprehension of the different vortex regeneration mechanism between the inner and outer walls proposed by Chung et al. (2002). It is worth mentioning that Brooke and Hanratty (1993) and Bernard et al. (1993) state that streamwise vortices entailing strong sweep motions can create other streamwise ones through the interaction with the wall. Since the surface area of the outer wall is larger than that of the inner wall, the regeneration process may be detected more violently. Due to the significant similarity between the flow and thermal fields, the investigation of the splat/anti-splat process may be also useful to clarify the different turbulent thermal structures between the inner and outer walls.

## 4. Summary and conclusions

In the present study, which is a continuation of the work presented by Chung et al. (2002), a DNS has been performed for turbulent heat transfer in a concentric annulus at $Re_{D_h} = 8900$ and $Pr = 0.71$ for two radius ratios ($R^* = 0.1$ and 0.5) and $q^* = 1.0$. Main emphasis is placed on the transverse curvature effect on near-wall turbulent thermal structures. At first, the Nusselt numbers and mean temperature profiles were represented to show and compare the mean thermal properties between near the inner and outer walls. It was found that the slope of the mean temperature profile near the inner wall was lower than that near the outer wall in the logarithmic region. Overall turbulent thermal statistics near the outer walls were larger than those near the inner walls due to the transverse curvature. This tendency was more apparent for small radius ratio. The limiting behaviors of the statistics were in excellent agreement with the previous DNS data. The cross-correlations between velocity and temperature indicated that the coherent thermal structures near the outer walls were stronger than those near the inner walls. The fluctuating temperature variance and turbulent heat flux budgets were illustrated to confirm the results of the lower-order statistics. The p.d.f.s of the splat/anti-splat process were scrutinized to provide a complete scenario of the transverse curvature effects on the flow and thermal fields in a concentric annulus. The present numerical results showed that the turbulent thermal structures near the outer wall were more activated than those near the inner wall, which may be attributed to the different vortex regeneration processes between the inner and outer walls.

## Acknowledgement

This work was supported by a grant from the National Research Laboratory of the Ministry of Science and Technology, Korea.

## References

Bernard, P.S., Thomas, J.M., Handler, R.A., 1993. Vortex dynamics and the production of Reynolds stress. J. Fluid Mech. 253, 385–419.

Brooke, J.W., Hanratty, T.J., 1993. Origin of turbulence-producing eddies in a channel flow. Phys. Fluids 5, 1011–1022.

Chung, S.Y., Rhee, G.H., Sung, H.J., 2002. Direct numerical simulation of turbulent concentric annular pipe flow. Part 1: Flow field. Int. J. Heat Fluid Flow 23, 426–440.

Dalle Donne, M., Meerwald, E., 1973. Heat transfer and friction coefficients for turbulent flow of air in smooth annuli at high temperatures. Int. J. Heat Mass Transfer 16, 787–809.

Eggels, J.G.M., Unger, F., Weiss, M.H., Westerweel, J., Adrian, R.J., Friedrich, R., Nieuwstadt, F.T.M., 1994. Fully developed turbulent pipe flow: A comparison between direct numerical simulation and experiment. J. Fluid Mech. 268, 175–209.

Hasan, A., Roy, R.P., Kalra, S.P., 1992. Velocity and temperature fields in turbulent liquid flow through a vertical concentric annular channel. Int. J. Heat Mass Transfer 35, 1455–1467.

Heikal, M.R.F., Walklate, P.J., Hatton, A.P., 1976. The effect of free stream turbulence level on the flow and heat transfer in the entrance region of an annulus. Int. J. Heat Mass Transfer 20, 763–771.

Kang, S., Patil, B., Zarate, J.A., Roy, R.P., 2001. Isothermal and heated turbulent upflow in a vertical annular channel—Part 1. Experimental measurements. Int. J. Heat Mass Transfer 44, 1171–1184.

Kasagi, N., Kuroda, A., Hirata, M., 1989. Numerical investigation of near-wall turbulent heat transfer taking into account the unsteady heat conduction in the solid wall. Trans. ASME: J. Heat Transfer 111, 385–392.

Kasagi, N., Tomita, Y., Kuroda, A., 1992. Direct numerical simulation of passive scalar field in a turbulent channel flow. Trans. ASME: J. Heat Transfer 114, 598–606.

Kawamura, H., Nakamura, S., Satake, S., Kunugi, T., 1994. Large eddy simulation of turbulent heat transfer in a concentric annulus. Thermal Sci. Eng. 2, 16–25.

Kawamura, H., Ohsaka, K., Abe, H., Yamamoto, K., 1998. DNS of turbulent heat transfer in channel flow with low to medium-high Prandtl number fluid. Int. J. Heat Fluid Flow. 19, 482–491.

Kim, J., Moin, P., 1989. Transport of passive scalars in a turbulent channel flow. In: Turbulent Shear Flows, vol. 6. Springer-Verlag, Berlin, pp. 85–96.

Kim, K., Baek, S.-J., Sung, H.J., 2002. An implicit velocity decoupling procedure for the incompressible Navier–Stokes equations. Int. J. Numer. Meth. Fluids 38, 125–138.

Kong, H., Choi, H., Lee, J.S., 2000. Direct numerical simulation of turbulent thermal boundary layers. Phys. Fluids 12, 2555–2568.

Kuzay, T.M., Scott, C.J., 1977. Turbulent heat transfer studies in annulus with inner cylinder rotation. Trans. ASME: J. Heat Transfer 99, 12–19.

Lu, D.M., Hetsroni, G., 1995. Direct numerical simulation of a turbulent open channel flow with passive heat transfer. Int. J. Heat Mass Transfer 38, 3241–3251.

Lyons, S.L., Hanratty, T.J., Mclaughlin, J.B., 1991. Direct numerical simulation of passive heat transfer in a turbulent channel flow. Int. J. Heat Mass Transfer 34, 1149–1161.

Malik, M.J., Pletcher, R.H., 1981. A study of some turbulence models for flow and heat transfer in ducts of annular cross-section. Trans. ASME: J. Heat Transfer 103, 146–152.

Mansour, N.N., Kim, J., Moin, P., 1988. Reynolds-stress and dissipation-rate budgets in a turbulent channel flow. J. Fluid Mech. 194, 15–44.

Moin, P., Kim, J., 1982. Numerical investigation of turbulent channel flow. J. Fluid Mech. 118, 341–377.

Na, Y., Hanratty, T.J., 2000. Limiting behavior of turbulent scaler transport close to a wall. Int. J. Heat Mass Transfer 43, 1749–1758.

Perot, B., Moin, P., 1995. Shear-free turbulent boundary layers. Part 1. Physical insights into near-wall turbulence. J. Fluid Mech. 295, 199–227.

Shen, L., Zhang, X., Yue, D.K.P., Triantafyllou, G.S., 1999. The surface layer for free-surface turbulent flows. J. Fluid Mech. 386, 167–212.

So, R.M.C., Sommer, T.P., 1996. An explicit algebraic heat-flux model for the temperature field. Int. J. Heat Mass Transfer 39, 455–465.

Tiselj, I., Bergant, R., Mavko, B., Baisic, I., Hetsroni, G., 2001a. DNS of turbulent heat transfer in channel flow with heat conduction in the solid wall. Trans. ASME: J. Heat Transfer 123, 849–857.

Tiselj, I., Pogrebnyak, E., Li, C., Mosyak, A., Hetsroni, G., 2001b. Effect of wall boundary condition on scalar transfer in a fully developed turbulent flume. Phys. Fluids 13, 1028–1039.

Velidandla, V., Putta, S., Roy, R.P., 1996. Turbulent velocity field in isothermal and heated liquid flow through a vertical annular channel. Int. J. Heat Mass Transfer 39, 3333–3346.

Wilson, N.W., Medwell, J.O., 1968. An analysis of heat transfer for fully developed turbulent flow in concentric annuli. Trans. ASME: J. Heat Transfer 90, 43–50.

Zarate, J.A., Roy, R.P., Laporta, A., 2001. Isothermal and heated turbulent upflow in a vertical annular channel—Part 2. Numerical simulations. Int. J. Heat Mass Transfer 44, 1185–1199.